chemengineering

MDPI

*Article*

# Parametric CFD Study of Spray Drying Chamber Geometry: Part I—Effects on Airflow Dynamics

**Jairo Andrés Gutiérrez Suárez [1,*,†], Carlos Humberto Galeano Urueña [2,†] and Alexánder Gómez Mejía [1,†]**

[1] Grupo de Investigación en Biomasa y Optimización Térmica de Procesos, Departamento de Ingeniería Mecánica y Mecatrónica, Facultad de Ingeniería, Universidad Nacional de Colombia-Sede Bogotá, Cra 45 #26-85, Bogotá 111321, Colombia; agomezm@unal.edu.co

[2] Grupo de Modelado y Métodos Numéricos en Ingeniería, Departamento de Ingeniería Mecánica y Mecatrónica, Facultad de Ingeniería, Universidad Nacional de Colombia-Sede Bogotá, Cra 45 #26-85, Bogotá 111321, Colombia; chgaleanou@unal.edu.co

* Correspondence: jaagutierrezsu@unal.edu.co

† These authors contributed equally to this work.

**Abstract:** Internal airflow dynamics play a crucial role in spray drying engineering by governing particle transport and, consequently, the quality of dried products. For this application, airflow dynamics represent short- and long-timescale behaviors across the main jet and recirculation regions and have been related, among other factors, to spray chamber design. This study examines the parametric effects of key geometrical design parameters on internal airflow dynamics using Design of Experiments (DOE) methodologies and 3D Computational Fluid Dynamics (CFD) simulations. The CFD model adopts a cost-efficient approach, including adaptive mesh refinement (AMR) methods, enabling running multiple simulation cases while retaining turbulence-resolving capabilities. The results provide quantitative parameter–response relationships, offering insights into the impact of chamber geometry on complex airflow behaviors. Among the parameters studied, the chamber aspect ratio strongly influences the strength of external recirculation flows. The inlet swirl primarily governs the stability of central and recirculating flows, while the conical–cylindrical section topology, in conjunction with the jet Reynolds number, affects flow impingement on walls, predominantly caused by the precession and reversal of the central jet. This methodology demonstrates significant potential for future studies on particle drying, equipment, process scale-up, and alternative chamber configurations in spray drying systems.

**Keywords:** spray drying; detached eddy simulation; computational fluid dynamics; parametric study; spray chamber geometry; airflow dynamics



Academic Editors: Yucheng Fu and Dewei Wang

Received: 2 September 2024
Revised: 22 November 2024
Accepted: 17 December 2024
Published: 4 January 2025

**Citation:** Gutiérrez Suárez, J.A.; Galeano Urueña, C.H.; Gómez Mejía, A. Parametric CFD Study of Spray Drying Chamber Geometry: Part I—Effects on Airflow Dynamics. *ChemEngineering* **2025**, *9*, 5. https://doi.org/10.3390/chemengineering9010005



## 1. Introduction

Predicting end-product quality is a common problem in spray drying processing [1], especially for heat-sensitive products such as foods and drugs. Generally, end-product quality in spray drying has been associated with different parameters, which are related to drying equipment design [2–4], operational parameters [5–8], or dependent on the properties of the feed product [3,9]. Drying equipment design parameters can be related to the size of the drying chamber (industrial, pilot, or lab sizes), the configuration of the drying chamber (co-current flow, counter-current, side-flow, etc.), and the geometry and shape (size relations, annular jet blockage ratio, swirl, etc.). Process operational parameters consist mainly of different process configurations (inputs), such as air inlet temperature, air

and feed mass flow, inlet humidity, and atomizer rotational speed. Feed product parameters include the properties of the carrier agent, such as the type and concentration, and the product properties.

Among these parameters, those related to geometry and design are the most challenging to study, as the effects of operational or feed product parameters can be tested directly during operation, while changes to geometrical or design parameters require systematic modifications to the equipment configuration or structure. Nevertheless, the importance of geometrical parameters is considerable, as they can significantly influence the quality of the final product by affecting the dynamics of various thermophysical phenomena within the drying chamber. The geometry of the drying chamber and the inlet diffuser have a major effect on the complex internal gas-flow dynamics [10–16] and consequently affect the turbulent dispersion of atomized particles [17,18]. Due to the turbulent dispersion, the particles take different paths and are subject to different dynamic and thermal behaviors, thus affecting the physicochemical, sensorial, and nutritional properties of the final product. Particles transported by improper gas flow patterns inside the drying chamber may cause roof and wall fouling, further deteriorating the end-product quality [19]. For these reasons, it is not possible to ensure that a selected set of operating parameters and feed-product characteristics designed for specific drying equipment will be adequate in a chamber of a different size or with different geometrical features. Despite the importance of geometrical parameters, their effects on flow characteristics has not been studied in sufficient depth, and the design of spray dryers still largely depends on empirical knowledge [20–22]. This makes studying the effects of these parameters relevant to spray drying technology.

Much of the knowledge regarding the effects of geometrical parameters on flow dynamics and the final product is based on qualitative observations. For example, it is well known that chamber size is related to the evaporation capacity of the equipment. For heat-sensitive products, which require short gas residence times, short-form dryers with a small chamber height-to-width ratio are most commonly used, as they can accommodate the comparatively flat spray disk from a rotary atomizer [20]. In contrast, tall-form chambers with a large height-to-width ratio are typically employed for non-heat-sensitive products, where thermal degradation is not a limiting factor. Despite these considerations, few studies describe quantitative flow responses as a function of an input variable. Lebarbier et al. [15] evaluated the direct effect of a parameter dependent on the air scattered geometry (swirl number) on a measurable response variable of the central jet precessing motion (dominant frequency). Keshani et al. [13] studied the effects of the curvature between the conical and cylindrical sections of the drying chamber on the shear stresses of the chamber. While these studies provide valuable insight into the potential effects of some geometrical design parameters, full parametric studies of normalized spray chamber geometries are needed to determine the individual and combined effects of different design parameters on flow-related response variables.

Conducting a parametric study of this nature presents two main challenges. The first is accurately modeling the inherently unstable nature of the airflow inside the drying chamber [10,14,15,23] which cannot be adequately captured using steady-state simulations, requiring a very costly transient modeling approach [24,25]. The costs of transient simulations are further increased by significant differences in the characteristic timescales of key airflow phenomena within the chamber, spanning up to six orders of magnitude [26,27]. These timescale differences range from microseconds in the inlet diffuser to seconds in the external recirculation zones and the precessing motion of the jet. Consequently, the number of time steps required to resolve these phenomena must be sufficiently long to allow the instabilities to develop [24], enabling the flow to reach its quasi-steady limits [10]. The second challenge is the parameterization of the problem, including the selection of

design parameters and response variables. The choice of these variables is not trivial and sometimes can be subjective [28]. For these reasons and to increase the rigorousness of the parametric study, it is convenient to use a DOE (Design of Experiments) methodology.

This study aims to evaluate the parametric effects of key geometrical design parameters of a spray drying chamber on internal airflow dynamics using CFD simulations. The airflow dynamics inside the chamber encompass both short- and long-timescale behaviors of the central jet and the external flow recirculation regions. DOE methodologies are employed to investigate the individual effects of each factor, as well as their interactions. This study will be complemented later by an expansion of the parametric evaluation to include the effects on particle histories.

Given the high computational cost associated with transient simulations of spray drying processes, this study adopts a cost-effective CFD modeling approach previously evaluated by the same authors [24,27]. This approach, suitable for industrial-scale simulations, includes the use of a low-cost, eddy-resolving turbulence model (DDES), enabling effective resolution of flow structures inside the drying chamber, capturing both short- and long-timescale phenomena. Additionally, adaptive mesh refinement strategies reduce simulation times and alleviate the computational load of the parametric study, making it feasible to explore more factors. By combining DOE methodologies with cost-effective CFD techniques, this study represents the first of its kind for spray drying applications.

This paper is divided into five sections. Section 2 presents the application of the DOE methodology to the CFD problem. Section 3 focuses on the methodology used to perform the computational implementation of the DOE using CFD, including the mathematical model, the grid construction, the solver configuration, and the post-processing algorithms. Section 4 presents the results and discussion based on the statistical analysis, and Section 5 presents the conclusions and recommendations.

## 2. Design of Experiments Methodology (DOE)

The DOE methodology used in this work is based in the general guidelines presented by Coleman and Montgomery [29] for industrial experiments and by Rhew and Parker [30] for parametric CFD modeling.

### *2.1. Objectives of the Numerical Experiment*

Using CFD to evaluate the effects of different geometrical design parameters of the spray chamber (factors) influencing the internal flow dynamics (response). The evaluation is conducted by quantifying the main effects and interactions of the factor variables over the response. As the response (airflow dynamics) is qualitative in nature, it must be described as a set of quantitative variables. The target results of this study are (1) to reduce the number of factor variables and interactions for similar future studies featuring atomization, evaporation, and the drying of liquid particles; (2) to support the design of co-current spray chambers through the understanding of the quantitative effects of different design parameters on the airflow behavior; and (3) to provide a reference methodology for future parametric CFD studies on spray chambers and similar devices.

### *2.2. Parametrized Geometry of a Spray Drying Chamber*

Figure 1 presents a proposed parametrized geometry of a typical co-current type spray drying chamber with the air disperser located at the top. This arrangement is the most widely used [31] and is suitable for drying heat-sensitive materials [17,32]. The air disperser provides an entrance for a high-velocity and -temperature swirling turbulent drying gas. In the present parametrized geometry, it has been largely simplified, as guide vanes are not included. The air enters radially ($U_r$), and the swirl is defined by the tangential component

of the air entering the disperser ($U_\theta$). This simplification in the annular inlet, proposed by García-Villalba et al. [33] and tested for spray drying applications in previous studies by the current authors [24,27], offers a reduced modeling complexity and significantly cuts down the costs of the CFD simulation. The parametrized air disperser geometry is constructed mainly in terms of the external and internal diameters of the jet ($D_o$, $D_i$).

The main design and construction parameters are the chamber diameter $D_c$ and the heights of the cylindrical $H_{cyl}$ and conical $H_{con}$ sections. The saggita of the arc (sag) represents a curvature parameter in the conical section. The air exits the chamber through an outlet duct of length $H_{ot}$ and diameter $D_{ot}$. Additional parameters for describing uncommon spray drying chamber geometries were presented by Huang et al. [12]; however, these were not included in this study because their practical application is unknown. Their evaluation can be conducted later, progressively, in accordance with the needs of process design and development, using the methodology proposed in this study.

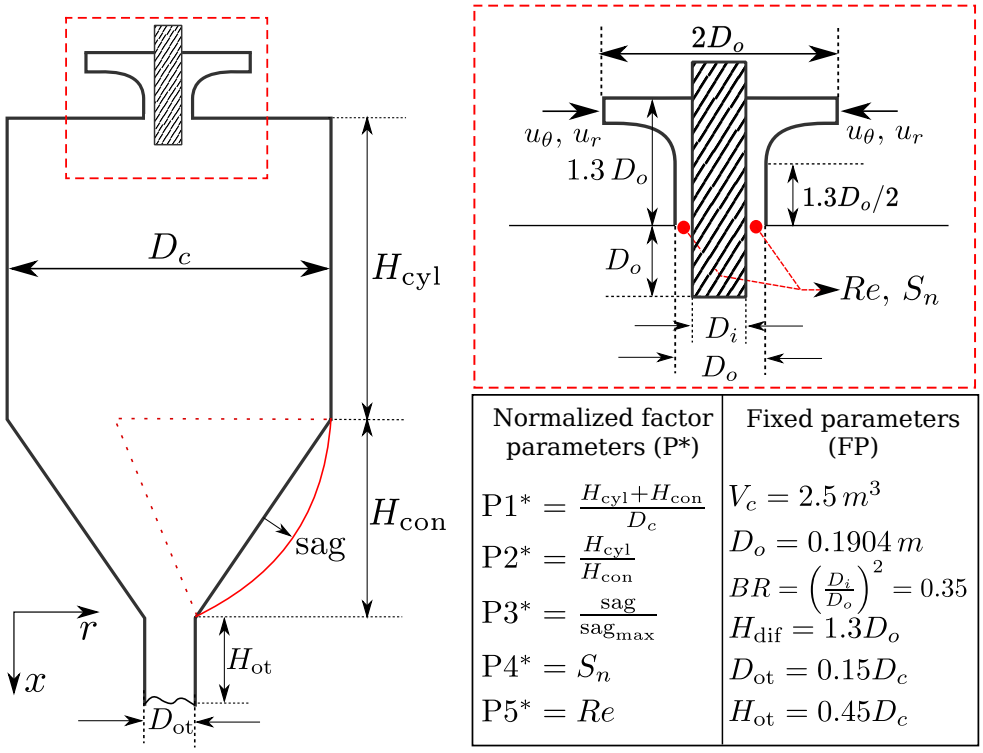


| Normalized factor parameters (P*) | Fixed parameters (FP) |
|---|---|
| $P1^* = \frac{H_{cyl}+H_{con}}{D_c}$ | $V_c = 2.5\,m^3$ |
| $P2^* = \frac{H_{cyl}}{H_{con}}$ | $D_o = 0.1904\,m$ |
| $P3^* = \frac{sag}{sag_{max}}$ | $BR = \left(\frac{D_i}{D_o}\right)^2 = 0.35$ |
| $P4^* = S_n$ | $H_{dif} = 1.3D_o$ |
| $P5^* = Re$ | $D_{ot} = 0.15D_c$ |
| | $H_{ot} = 0.45D_c$ |

**Figure 1.** Parametrized geometry with factors and fixed parameters used in the DOE study.

### *2.3. Factor Parameters*

The factor parameters $P^*$ are presented in Figure 1. From $P1^*$ to $P4^*$, they represent a non-dimensional form of the main geometrical parameters of the construction of the spray dryer. $P1^*$ is the height-to-width ratio of the chamber and is frequently mentioned in the literature. For short-form chambers (low $P1^*$ values), this parameter affects the transient flow behavior [16] as stronger flow instabilities are likely to develop [10]. $P2^*$ is the height ratio of the cylindrical and conical sections of the drying chamber. According to Huang et al. [12], this relation has a strong effect on the positioning of the recirculation zone, which in turn affects flow stability and particle transport. $P3^*$ defines if the chamber has a straight or parabolic bottom section. The effects of this factor are discussed in Keshani et al. [13], where its important effects on flow uniformity and particle deposition on the walls are

highlighted. $P4^* = S_n$ is the swirl number measured at the jet discharge, which depends on the geometrical design of the air disperser and its guide vanes. $P4^*$is calculated as

$$P4^* = S_n = \frac{\int_0^{R_o} \rho U_x U_\theta r^2 dr}{R \int_0^{R_o} \rho U_x^2 r dr}, \quad (1)$$

relating the axial and tangential momentum $\rho U_x U_\theta$ to the axial momentum $\rho U_x^2$ across all radial sections ($R$). In spray drying applications, this factor plays a key role in the stability of the internal flow [15] and may contribute to a higher drying efficiency at the expense of increased particle deposition on the walls [28]. In spray dryers with a rotary atomizer, the amount of swirl at the discharge may be increased due to the rotating motion of the disk [18].

The last parameter, $P5^* = Re$, represents the Reynolds number at the jet discharge. For a fixed air disperser design, increased $P5^*$ values are associated with higher temperatures and/or increased volumetric flows of the drying air. While this parameter is not geometric but rather operational, its inclusion in this study enables a comprehensive evaluation of the interactions between geometric parameters and operational conditions. Specifically, it facilitates the assessment of how the Reynolds number of the jet might modulate the effects of geometric design parameters on internal airflow behavior. To illustrate this, according to Pawar [34], higher $Re$ values increase the penetration of the jet into the drying chamber, which causes a stronger shear region between the jet and its surroundings. In this case, it is not completely clear how other parameters (e.g., $P1^*$) would affect this interaction, as increasing $P5^*$ values in a tall-form (narrow) chamber could promote jet impingement with the walls, disrupting the interaction between the central jet and its surroundings.

### 2.4. Ranges of Factor Parameters

The ranges of the factor parameters are presented in Table 1. To incorporate reasonable range values, chamber geometry, and operational parameters, data reported in the literature [1,14,16,35,36] were used as references and are summarized in Table 2. For P4*, the ranges are based on those studied by Langrish et al. [14] since the values reported by other studies are not fully representative of actual operating conditions. This is exemplified in Kieviet and Kerkhof [37], where the swirl vanes of the air disperser were removed before carrying out the measurements.

The direct calculation of the ranges of $P5^*$ using the literature data is inadequate, as the Reynolds number varies significantly with the drying chamber size and annular entrance geometry, both of which are fixed parameters in the experimental design. For this reason, a chamber fill-time parameter, $t_f = \frac{V_c}{\dot{v}}$, was first defined, where $V_c$ is the volume of the drying chamber and $\dot{v}$ is the volumetric flow rate of inflowing air. This new parameter $t_f$ is independent of other geometric parameters and, for practical purposes, relates the chamber size to its drying capacity. Once the ranges of $t_f$ are determined using the literature data, it is possible to calculate the Reynolds numbers specific to the chamber volume and air disperser topology defined for the experimental plan, as presented in Table 2.

**Table 1.** Ranges of factor parameters.

| Parameter | Middle Value | max. | min. |
|---|---|---|---|
| P1* | 1.68 | 2.5 | 1.2 |
| P2* | 1.60 | 2.0 | 0.5 |
| P3* | 1.75 | 1 | 0 |
| P4* | 0.25 | 0.5 | 0.05 |
| P5*($\times 10^4$) | 4.2 | 7.0 | 2.8 |

**Table 2.** Determination of typical ranges for the factor parameters, using as a reference the values reported in the literature for different pilot-size and semi-industrial-size spray chambers.

| Reference | P1* | P2* | P3* | P4* | $t_f$(s) | P5*($\times 10^4$) |
|---|---|---|---|---|---|---|
| Kieviet and Kerkhof [37] | 1.68 | 1.16 | 0 | 0.09 | 19.73 | |
| Huang et al. [35] | 1.60 | 0.88 | 0 | 0 | 23.54 | |
| Woo et al. [16] | 1.75 | 0.67 | 0 | 0 | 8.60 | |
| Langrish et al. [14] | 2.01 | 1.56 | 0 | 0.45 | 14.36 | |
| Gutiérrez Suárez [36] | 1.77 | 1.15 | 0 | 0.10 | 10.25 | |
| Average | 1.76 | 1.08 | 0 | 0.13 | 15.30 | 4.2 |
| Maximum | 2.01 | 1.56 | 0 | 0.45 | 23.54 | 2.8 |
| Minimum | 1.60 | 0.67 | 0 | 0 | 8.60 | 7.0 |

### *2.5. Fixed (Held Constant) Parameters*

The fixed parameters are presented in Figure 1 and include the chamber volume, air disperser dimensions, and outlet tube proportions. The chamber volume was set to $V_c = 2.5\,\mathrm{m}^3$, representing the average volume of the small-scale spray chambers listed in Table 2. While scaling the process to industrial capacities by progressively increasing $V_c$ is desirable, achieving this requires a more robust methodological approach. This challenge arises from the lack of dynamic similarity between small- and large-scale drying chambers, particularly in terms of gas flow patterns, turbulence modeling, and particle dynamics [4,38]. Consequently, the CFD models and grid arrangements considered in this study would need to be validated for higher Reynolds number ranges, with the added difficulty of the lack of experimental measurements on industrial-scale equipment. Therefore, evaluating the volumetric variation during process scale-up is a critical step that should be explored in future studies.

The other fixed parameters are related to the air disperser and outlet tube geometries. The air disperser incorporates an annular duct with $D_\mathrm{o}$ = 0.1904 m. This value was obtained from the mean expansion ratio ($D_\mathrm{o}/D_\mathrm{c}$) of spray chambers presented in Table 2. The blockage ratio $D_i^2/D_\mathrm{o}^2 = 0.35$ was selected considering the computational resources and the number of simulations to be performed. This parameter governs the computational cost of the simulation, and by increasing it, the grid elements in the discharge become smaller, and as a consequence, the time step becomes shorter. The rest of the air disperser geometry, including the top of the duct, is obtained using the same size and shape ratios used by Gutiérrez Suárez et al. [27]. For the outlet duct, fixed proportions are used for its diameter, which is related to the chamber diameter as $D_\mathrm{o,t} = 0.15D_\mathrm{c}$, and its length, which is related to its diameter as $H_\mathrm{o,t} = 0.45D_{o,t}$.

### *2.6. Response Variables*

Due to the nature of the computational simulation, which allows for measuring the responses at any point within the domain, the internal flow dynamics is represented in this study as a series of quantitative response variables. These variables are defined for two primary zones within the drying chamber previously identified by Hammad et al. [39], represented by the central jet (R-1) and the main recirculation zone (R-2). Within these zones, eight key response variables are determined—five in zone R-1 (R-1.1 to R-1.5) and three in zone R-2 (R-2.1 to R-2.3). The positioning of these zones in a simplified drying chamber is presented in Figure 2, while a detailed description, including response modes, is shown in Table 3.

The central jet (R-1) is dominated by a high-velocity annular jet-like flow. The response variables of this zone are directly associated with those of confined annular jets and are described here. The recirculation vortex length (R-1.1) indicates the extent of the recirculation zone beneath the bluff body and is defined as the point where $U_x = 0$. This

length can be expressed in terms of the outer radius of the annular jet $(x/R)$ or a normalized length based on the height of the drying chamber $(x/H)$. The extent of R-1.1 may be related to the jet decay, which is quantified in R-1.2. The jet decay is measured as a distance ($x/R$ or $x/H$) where the mean axial velocity at the centerline decreases to 0.6 $U_b$. Since decay alone does not fully indicate the extent of the jet relative to the chamber height, an additional response is measured. This response is calculated as $U_x/U_b$ at $x/H = 0.5$ and represents the jet penetration into the chamber (R-1.3), which is normalized by the chamber height. In this manner, a separate analysis of the absolute jet decay and its relative value to the drying chamber is performed.

For the same normalized axial position used to read R-1.3 ($x/H = 0.5$ in the axis), three additional response variables are measured,as follows: the *rms* fluctuations of the axial velocity (R-1.4) and the dominant frequency characteristics (R-1.5). The *rms* fluctuations of the axial velocity (*rms* $U_x/U_b$) indicate the amount of turbulence in the central jet and can be related to its decay and stability. The dominant frequency response parameter R-1.5 is calculated using a Fourier Fast Transform (FFT $U_x$). This analysis aims to process velocity-time signal data into a frequency spectrum, as discussed by Woo et al. [16]. The frequency spectrum data are used to determine the existence or absence of precession in the main jet. According to Southwell and Langrish [40], the oscillations arising from such precessions within a large expansion should be avoided in spray dryers because they tend to cause undesirable back-mixing and particle deposition on walls, ruining the quality of the products. The results of this analysis will determine how the precession in the central flow is affected by geometric factors of the chamber, regardless of the amount of swirl at the jet discharge.

The main recirculation zone (R2) is located between the periphery of the central jet and the walls of the drying chamber. In this zone, part of the central flow changes direction and circulates upwards. The response variables for the characterization of this zone are as follows: the recirculation force (R-2.1) represents the ratio between the recirculation flow rate $\dot{Q}_r$ and the bulk flow rate $\dot{Q}_b$. For confined jets, it is strongly dependent on the expansion ratio $D_c/R_o$. The axial position of the maximum recirculation flow (R-2.2) normalized by the chamber height $(x/H)$ indicates the axial position of the axis about which the recirculation vortex rotates. This position is also related to the turning point of the jet described in Pawar [34]. The stability of the recirculating flow is studied by the strength of its *rms* fluctuations (R-2.3), which is computed at the axial position obtained in R-2.2. The strength of the fluctuations in the recirculation region has a double effect on the wall deposition of particles. Large flow instabilities tend to increase the number of deposited particles, but turbulent gusts near the walls significantly impact their removal and reincorporation.

### 2.7. Nuisance Factors

The numerical solution obtained from CFD is deterministic. The same numerical models, discretization schemes, and solution algorithms are consistently applied across all experiments. Since this study does not employ numerical sub-models with stochastic components, they do not introduce a nuisance factor. The primary nuisance factor in this study is the challenge of maintaining a consistent distribution of discretization errors across the domain in the various experiments. This inconsistency arises from the different geometrical and operational configurations (e.g., increasing P5* increases the shear stresses in the jet). To mitigate this nuisance factor, the grid construction downstream and outward from the jet discharge was standardized. Additionally, adaptive mesh refinement (AMR) was employed to further address this issue by reducing discretization errors through targeted grid refinement, as detailed in Section 3.

**Table 3.** Description of the response variables used in the parametric study.

| Response Variables | | | |
|---|---|---|---|
| **Flow Region** | **Name** | **Description** | **Response Form and Location** |
| **Central jet (R1)** | R-1.1 | Length of the internal recirculation vortex, described in [39,41] as part of the near-field of the jet. | $x/H$ and $x/R$ at $U_x = 0$ |
| | R-1.2 | Jet decay along the axis. It is affected by P4* [14]. May be affected by P5* [34]. | $x/H$ and $x/R$ at $U_x = 0.6U_b$ |
| | R-1.3 | Penetration of the jet in the drying chamber, normalized to the bulk velocity. It decreases as P4* increases P4*[14]. | $U_x/U_b$ at $x/H = 0.5$ |
| | R-1.4 | Turbulence in the jet axis. | rms $U_x/U_b$ at $x/R = 10$ and $x/H = 0.5$ |
| | R-1.5 | Dominant frequency: R-1.5.1: frequency and R-1.5.2: amplitude, which are affected by P1* [34] and by P4* [15]. | R-1.5.1: $H_z$ $U_x$ at $x/H = 0.5$, R-1.5.2: Amplitude ($m$) at $x/H = 0.5$. |
| **External recirculation zone (R2)** | R-2.1 | Recirculation strength. It may be related to wall shear stresses and particle–wall interactions [3]. It is affected by swirl (P4)* [28]. | max $\dot{Q}_r/\dot{Q}_b$ in the axial direction in R2 |
| | R-2.2 | Position of the recirculating flow. It may be affected by P5* [34]. | Position ($x/R$ or $x/H$) of R-2.1 (max $\dot{Q}_r/\dot{Q}_b$) (R-2.1) |
| | R-2.3 | Stability of recirculating flow. It may be related to P3* [13] and affects particle deposition on walls. It may also affect the detachment of dried particles [39]. | rms $U_x$ at $x/H$ predicted by R-2.2 |

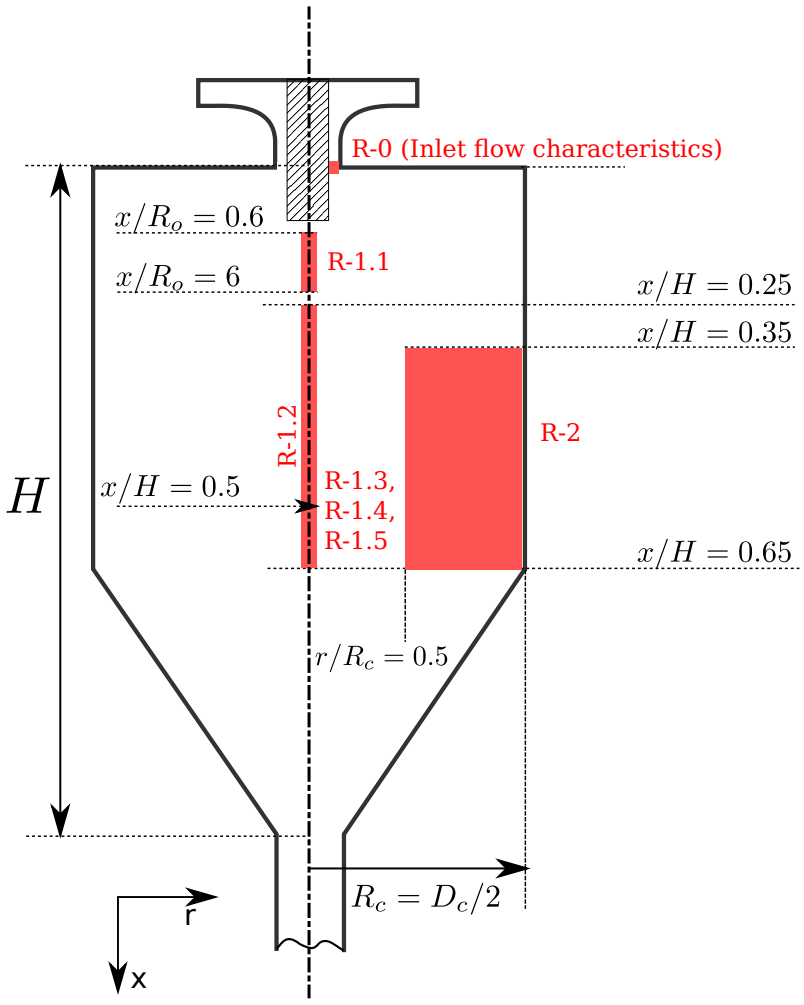


**Figure 2.** Measurement regions inside a normalized drying chamber, including the jet discharge (R-0), central jet (R-1), and external recirculation (R-2) regions. Details of R-1 and R-2 are provided in Table 3.

### 2.8. Spreadsheet of Experiments

A fractional factorial design was used to study the factor–response interaction. A detailed description of this design type is presented in Montgomery [42]. The fractioning reduces the number of experimental runs over the factors where a detailed response analysis is not required. In this case, P5*, which does not represent a geometric but an operational factor, was set as the fractional factor. The number of levels and fractional factors also depend on the computational resources available and the cost of running each experiment. Given the costs reported in a previous study by the same authors [24] and the available resources, a $2^{5-1}$ design consisting of 16 experiments was proposed. The 2-level design was sufficient for the scope of this study, which is exploratory. A 3-level study was not considered since maintaining the number of experiments would have required a reduction in the number of factorial parameters. However, an additional experiment using intermediate values was included to evaluate the curvature in the response. The resulting spreadsheet of experiments is presented in Table 4.

**Table 4.** Spreadsheet of numerical experiments.

| Experiment | P1* | P2* | P3* | P4* | P5* ($10^4$) |
|---|---|---|---|---|---|
| 1 | 1.2 | 0.5 | 0 | 0.05 | 7.0 |
| 2 | 2.5 | 0.5 | 0 | 0.05 | 2.8 |
| 3 | 1.2 | 2 | 0 | 0.05 | 2.8 |
| 4 | 2.5 | 2 | 0 | 0.05 | 7.0 |
| 5 | 1.2 | 0.5 | 1 | 0.05 | 2.8 |
| 6 | 2.5 | 0.5 | 1 | 0.05 | 7.0 |
| 7 | 1.2 | 2 | 1 | 0.05 | 7.0 |
| 8 | 2.5 | 2 | 1 | 0.05 | 2.8 |
| 9 | 1.2 | 0.5 | 0 | 0.5 | 2.8 |
| 10 | 2.5 | 0.5 | 0 | 0.5 | 7.0 |
| 11 | 1.2 | 2 | 0 | 0.5 | 7.0 |
| 12 | 2.5 | 2 | 0 | 0.5 | 2.8 |
| 13 | 1.2 | 0.5 | 1 | 0.5 | 7.0 |
| 14 | 2.5 | 0.5 | 1 | 0.5 | 2.8 |
| 15 | 1.2 | 2 | 1 | 0.5 | 2.8 |
| 16 | 2.5 | 2 | 1 | 0.5 | 7.0 |
| 17 | 1.85 | 1.25 | 0.5 | 0.275 | 4.2 |

## 3. Numerical Methods and Computational Configuration

### 3.1. Governing Equations and Turbulence Modeling

The time-dependent cold flow field for all the numerical experiments is solved using transient, incompressible, unsteady Navier–Stokes equations, adopting unsteady RANS and filtered (LES) formulations through the domain. The transport equations for continuity (Equation (2)) and momentum (Equation (3)) for the given modeling strategy are

$$\frac{\partial u_i^*}{\partial x_i} = 0 \tag{2}$$

$$\frac{\partial u_i^*}{\partial t} + \frac{\partial \left(u_i^* u_j^*\right)}{\partial x_j} = -\frac{1}{\rho}\frac{\partial p^*}{\partial x_i} + \left([\nu + \nu^*]\frac{\partial u_i^*}{\partial x_j}\right). \tag{3}$$

Under RANS mode, an averaging operation is performed as $\phi_n^* = \langle \phi_n \rangle$ and the viscosity term $\nu^*$ becomes the turbulent viscosity $\nu_T$. In LES mode, spatial filtering is used with $\phi_n^* = \overline{\phi_n}$, and the viscosity term $\nu^*$ is replaced by the sub-grid scale (SGS) viscosity with $\nu^* = \nu_{SGS}$. Details on the averaging and spatial filtering operations can be consulted in Davidson [43]. For both modes of operation the model viscosity $\nu^*$ is calculated using a DDES turbulence model [44]. The cold-flow conditions are defined as a non-reacting single-phase gas with a kinematic viscosity of $\nu = 1.48 \times 10^{-5}\,\mathrm{m^2/s}$ and a density of $\rho = 1.16\,\mathrm{kg/m^3}$, representing dry air at 15 °C.

### 3.2. Numerical Schemes and Methods

The governing equations (Equations (2) and (3)) were discretized and solved using the open-source CFD software OpenFOAM V1706, running a modified version of the solver pimpleDyMFoam, which incorporates a customized mesh adaptation criterion described in the next section. The numerical schemes and discretization methods employed were the same as those evaluated in a previous study (see Gutiérrez Suárez et al. [24]) and are summarized in Table 5. All temporal and spatial terms were second-order accurate. div($\phi$) used a hybrid scheme [45] which blended linear-upwind differencing (LUD) with a central-differencing scheme (CDS) depending on the mode of operation (RANS or LES). The pressure–velocity coupling was managed by the PIMPLE algorithm (for details, see Holzmann [46]). The simulation time step was dynamic, controlled by the maximum flow Courant number, which was set to 0.85. This value is typically reached near the jet discharge and represents a good balance between performance and accuracy, as it limits the generation of artificial fluctuations. For pressure and velocity, the solver settings for residual control included a tolerance of $1.0 \times 10^{-5}$, a relative tolerance of 0.001, and a maximum of 10 iterations per outer PIMPLE loop.

**Table 5.** Numerical schemes and coupling methods reported by Gutiérrez Suárez et al. [24] and used in the present study.

| Schemes | Description |
|---|---|
| Temporal terms | SUOE *(Adams Moulton)*, second-order implicit. Described in Moukalled et al. [47]. |
| Gradient-$\nabla\phi$ | CDS *(central differencing scheme)* |
| Gradient-$\nabla \boldsymbol{u}$ | Limited-CDS |
| Advective terms-div($\phi$) | Hybrid scheme, described in Gutiérrez Suárez et al. [27], Travin et al. [45] |
| RANS mode | LUD *(linear upwind differencing)* |
| LES mode | CDS *(central differencing scheme)* |
| Pressure–velocity coupling | PIMPLE algorithm, described in Holzmann [46]. |

### 3.3. Adaptive Mesh Refinement (AMR)

To reduce simulation runtimes and alleviate the computational costs of the parametric study—thus enabling running as many numerical experiments as possible—a grid adaptation method based on the relative error of the velocity gradient was used. The general concepts of the relative error method are detailed in Bathe and Zhang [48], while its detailed implementation, parameter calibration, and evaluation in CFD simulations of spray dryers has been performed in a previous study [24]. Under this AMR criterion, any cell in the domain can be refined if its relative error $C_{\mathrm{rel}}$ is greater than a refinement criterion $C_{\mathrm{crit}}$. The relative error is calculated for each cell in terms of a local error indicator in the cell $c_l$ and the average of the error indicator in the domain $c_{\mathrm{avg}}$ as

$$C_{\text{rel}} = Re\frac{c_l}{c_{\text{avg}}} = \frac{\Delta_l \|\nabla U\|}{\frac{1}{N_e}\sum_e \Delta_l \|\nabla U\|}. \quad (4)$$

In the above equation, $\Delta_l$ is the mean edge length of the cell, $\|\nabla U\|$ is the norm of the velocity gradient, and $N_e$ is the number of elements in the domain. The other AMR parameters were also selected according to the findings of the aforementioned study. These parameters are a refinement threshold of two buffer cells, a refinement interval of 5 time steps, a base grid with a sufficient number of elements to activate AMR in the lower region of the jet, a maximum grid refinement level of 1, and an adapted-element ratio of around 30%. This parameter is calculated by comparing the current number of elements in the domain (after refinement) with the maximum possible number of elements (if all elements were refined to the maximum level).

### 3.4. Grids

For all numerical cases, the grids are fully structured and constructed using multiple blocks with curved edges. Figure 3 presents two examples of the base computational grids used. These grids are very coarse, ranging from 10,500 to 13,700 elements depending on the experimental case. Upon activation of AMR, this number increases to a maximum of 300,000 elements, as limited by the AMR settings described in the previous section. The elements are primarily concentrated around the jet discharge and outlet pipe regions. From the jet discharge, a positive growth factor was applied in the radial and axial directions, where the eddies are smaller in size and the associated turbulent kinetic energy is higher. As the eddies grow in size, the grid requirements for capturing turbulence decrease. The grid structure is detailed around the jet discharge (red dashed line) and the upper recirculation zone (blue dot-dashed line). In the latter, part of the block construction is shown in detail (blue lines). X1, X2, X3, and R1, R2, and R3 indicate cell-expansion ratios in the axial and radial directions for each blockMeshDict construction block. For all cases X1 = 1, X2 >1, X2 < 1, R1 = 1, R2 > 1, and R3 = 1.

A grid independence study was not explicitly conducted, as previous investigations have already assessed it for both the air disperser and the complete drying chamber by performing simulations with similar topologies, grid arrangements, and comparable flow conditions. In Gutiérrez Suárez et al. [27], grid independence was verified for mean and fluctuating velocity values in the near region of the jet, including the air disperser section. This region is critical as the low timescale flow phenomena occurring here govern the large-scale flow motion and unsteady behavior within the chamber. Therefore, in this study the same topology and grid element distribution of the air disperser and near-jet region was implemented. For the grid of the complete drying chamber, Gutiérrez Suárez et al. [24] have previously evaluated grid independence for fixed and dynamic grid configurations, including different settings of the mesh adaptation algorithm and their effects on the mean velocity and turbulence resolving capabilities.

The mesh settings are defined using a grid construction dictionary created for this purpose and allowing parametric operation. It utilizes the blockMeshDict and the codeStream classes of OpenFOAM to dynamically compile the code and parameterize the grid creation operations in terms of P1*, P2*, P3*, and the fixed parameter values. To reduce discretization errors across different experiments, the grid elements near the inlet are maintained at a consistent size. Additionally, the expansion ratio of cells in both the axial and radial directions (from the jet discharge) remains consistent across all experiments. Given the significantly varying flow conditions in the flow recirculation region across different geometries, maintaining a correct y+ value is challenging. To address this issue, the size of the first element was set around $y^+ = 100$, considering a mean flow velocity of

0.5 m/s. Gutiérrez Suárez et al. [24] showed that when the AMR velocity gradient criterion is used, these wall elements are automatically refined during turbulent bursts or at high flow velocities. This allows the $y^+$ value to remain within acceptable ranges.

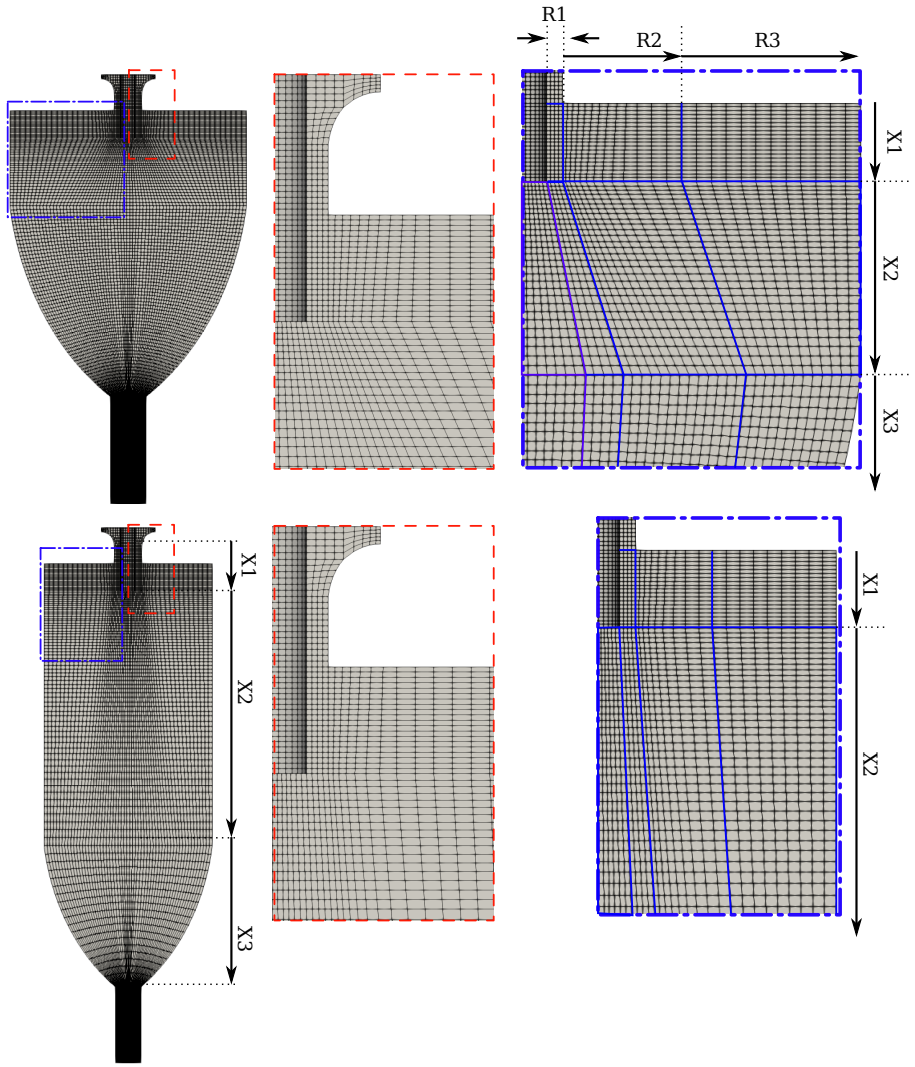


**Figure 3.** Computational grids for Experiments 5 and 13 (**top**) and Experiments 8 and 16 (**bottom**), including mesh details around the jet discharge and upper recirculation region.

### *3.5. Base Computational Configuration*

#### 3.5.1. Boundary Conditions

The boundary conditions and assumptions are consistent with those reported by Gutiérrez Suárez et al. [27] for the air disperser and by Gutiérrez Suárez et al. [24] for the rest of the drying chamber. Please refer to the studies for a more detailed discussion. The air velocity at the air disperser is specified using fixed-value vectors in cylindrical coordinates, defined by the tangential and radial velocity components, as shown in Figure 1. The magnitude of the radial component is set depending on the Reynolds number (P5*), while the tangential velocity $U_\theta$ is adjusted to produce a swirl number equal to P4* at the jet discharge (±1.5% P4*). Turbulent variables ($k$, $\omega$) are prescribed in the inlet with very low values ($1 \times 10^{-6}$), as the turbulence is developed through the simplified inlet duct [33]. In the walls, no-slip conditions are applied for the velocity, and the boundary layer treatment uses standard wall functions. For the outlet, a zero-gradient boundary condition is applied to the velocity and turbulence variables. The pressure in the outlet is defined through a fixed-value B-C, with $p_{\text{outlet}} = 0$.

3.5.2. Construction of the Computational Cases

The computational cases for all the experiments were generated using a script written in an open-source programming language (GNU-Octave). The script performs the following tasks:

- Reads the spreadsheet of experiments presented in Table 4 and a list of fixed parameters.
- Calculates the chamber dimensions for each case by an iterative procedure ($H_{cyl}$, $H_{con}$, $D_c$) and the position of the supporting vertices to create the conic-section of the chamber.
- Writes the mesh and boundary conditions configuration dictionaries.
- Writes the probe configuration file for each case, since some probe positions are relative to the chamber geometry.

3.5.3. Running Setup and Sampling of Data

The simulation times are defined in terms of a non-dimensional characteristic time $t_c = t_s/t_f$, where $t_s$ is the simulated time and $t_f$ is the fill-time. All the experiments were started at $t_c = 0$ and were run until $t_c = 3.5$ using the base grid (AMR off). At $t_c = 3.5$, AMR is activated, and the simulations are run until $t_c = 4.5$, when the probe sampling is activated, ending at $t_c = 6.5$. This methodology, procedure and simulation times are based on the results of Gutiérrez Suárez et al. [24].

3.5.4. Sampling and Post-Processing of Data

A total of 485 probes were used to sample data across different axial and radial regions in each numerical experiment. These probes were distributed throughout the measurement regions previously described in Figure 2, and are detailed as follows:

- The probes (12) located in R-0 were used to measure the axial velocity and swirl values at the entrance to the chamber. The collected data were used to calibrate the bulk velocity $U_b$ and swirl number $S_n$ at the discharge of the jet.
- The probes (61) located in R-1 zone were used to measure the response variables R-1.1 to R-1.5 and were located along the axial direction and $r/R_c = 0$. The probes in R-1.1 (20) were distributed from $x/R_o = 0.6$ to $x/R_o = 6$ and were used to capture information related to the recirculation vortex length. The probes in R-1.2 (40) were used to assess the decay of the jet ($x/H$ at $U_x = 0.6U_b$) and were distributed from $x/H = 0.25$ to $x/H = 0.65$. The last probe was located at $x/H = 0.5$ and was used to determine the penetration of the jet (R-1.3) to measure the *rms* fluctuations of the axial velocity (R-1.4) and to calculate the dominant frequency of the jet (R-1.5).
- The probes (400) located in R-2 (recirculation zone) were arranged in a squared grid ($20 \times 20$) from $x/R_c = 0.5 \rightarrow 1.0$ and $x/H = 0.35 \rightarrow 0.65$. These ranges were considered sufficient to capture the principal features of the recirculation zone.

All the probe data were post-processed using GNU-Octave. For R-1.1, R-1.2, and all variables in R-2, polynomial interpolation was used to estimate the values between the probes and calculate the required quantity for the response variable. Matlab functions (DOE-Plots) were used to perform the statistical analysis using the response data.

## 4. Results and Discussion

### *4.1. Computational Costs*

All computational simulations for the numerical experiments were performed on the JFF2 cluster at the Heat and Mass Transfer Technological Center (CTTC) of the Polytechnic University of Catalonia. For additional information on the cluster, see Gutiérrez Suárez et al. [24]. Each numerical experiment (case) utilized six physical processors, which helped maintain an optimal range of cells per processor, thereby reducing

bottleneck effects associated with parallel computing (see Culpo [49] for further details). The total computational cost, including both test and final cases, amounted to approximately 94,000 processor hours, equivalent to around 120 days when utilizing all 32 available processors.

### 4.2. Velocity Fields and Sampled Data

#### 4.2.1. Velocity Fields and AMR

Figure 4 presents the velocity field and computational grid for Experiment 8 at different simulation times. The resolution of turbulence (detached eddies) downstream of the discharge and the deflection of the jet towards the sides of the drying chamber were observed. This behavior was captured dynamically using the AMR method. Grid refinements in near-wall elements were observed during instances of pronounced jet deflection. ($t_c$ = 5.03; 5.7). Upstream of the discharge, constant refinement was present at all times. This acceptable dynamic refinement behavior was observed in all the simulations.

#### 4.2.2. Examples of Sampled Data

Figure 5 presents examples of sampled and post-processed data for Experiments 3 and 15. Figure 5a shows axial velocity measurements ($U_x$) along the axis at $x/H = 0.5$. It was observed that for Experiment 15 (P4* = 0.5), there was a significantly higher decay of the central jet than for Experiment 3 (P4* = 0.05), presenting in many cases negative velocities. Figure 5b shows the 2D velocity vectors obtained by averaging the recirculation zone (R-2) data, which were collected by 400 probes arranged in a 20 × 20 array, as shown in Figure 2. It was observed that the position of the recirculation vortex (R-2-2) was slightly higher (closer to the discharge) for Experiment 15 (P4* = 0.5).

Regarding the recirculation flow, Experiment 3 presented a larger area of recirculated flow but with a lower velocity than that shown in Experiment 15. In this case, the post-processing script performs the calculation of the total recirculated flow rate to determine R-2.1. Figure 5c) presents the results of an FFT (hann window) of the axial velocity ($U_x$) at $x/H = 0.5$. From the application of this FFT, the responses R-1.5.1 and R-1.5.2 (frequency and amplitude of the dominant frequency) were obtained. In Experiment 15 (P4* = 0.5), the dominant frequency greatly differed from other frequencies, as its amplitude was significantly higher. In this case, the other frequencies represent noise in the signal. In contrast, for Experiment 3, the difference in the amplitude presented by the dominant frequency and that of other spectrum frequencies was smaller. This difference was obtained because higher swirl numbers in the jet discharge generate a more distinct dominant frequency.

### 4.3. Main Effects and Pareto Plots

Figure 6 presents DOE plots for different response variables. The left column shows the main effects plot, and the right column the Pareto chart, where the horizontal blue line defines a 95% confidence interval ($P = 0.05$), $\alpha$ is the physical value of the threshold (in terms of the response variable) for the confidence interval, and $SS_T$ is the sum of squares. Figure 6a presents these plots for responses related to a physical distance (x/R), while Figure 6b,c present plots for responses normalized or at normalized positions for the central zone (R-1) and recirculation zone (R-2), respectively. The effects for each of the response variables are summarized below.

#### 4.3.1. R-1.1—Length of Internal Recirculation Vortex ($x/R$ & $x/H$)

The physical length of the recirculation vortex ($x/R$), presented in Figure 6a, is directly affected by the parameter P4* (swirl number). Normalizing this distance to the chamber height ($x/H$), the parameter P1* becomes statistically significant (see Figure 6b). It is obtained from this that increasing the swirl number impacts the size of the internal

recirculation zone. At $x/H = 0.5$, the value of the axial velocity is close to 0 when P4* = 0.5. This result is similar to that reported by Southwell and Langrish [28] in a pilot-size drying chamber with P4* = 0.45.

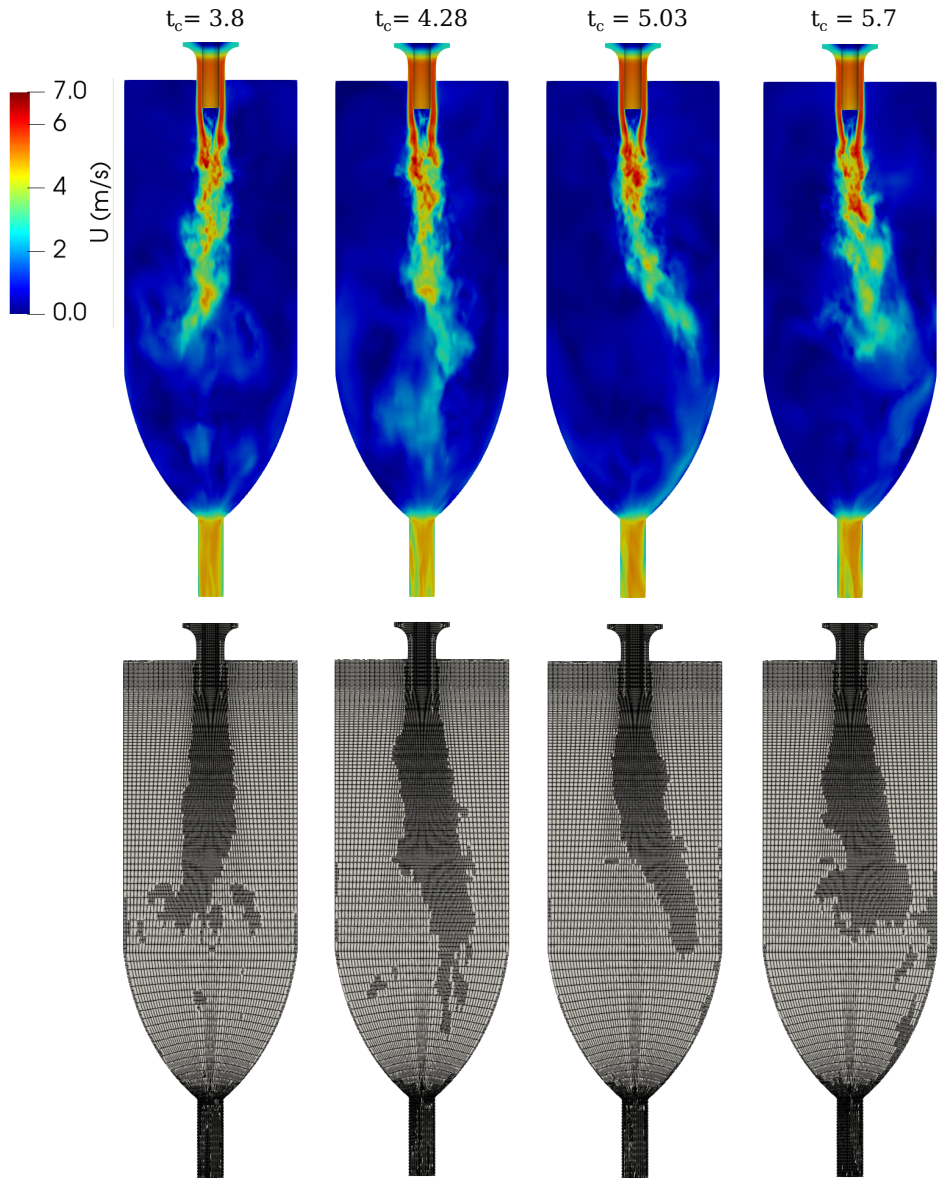


**Figure 4.** Unsteady flow and dynamic mesh behavior for Experiment 8. (**Top**): A 2D-cross section of the drying chamber showing velocity contours at different characteristic times. (**Bottom**): Mesh adaptation behavior at different characteristic times.

#### 4.3.2. R-1.2—Distance ($x/R$ & $x/H$) for the Jet to Decay to 0.6 $U_b$

The responses for the physical and normalized distances are presented in Figure 6a,b. For this response, the results of the effect of P4* were not included. This is because the effect of the swirl was so strong that when P4* = 0.5, the jet decayed very quickly, and values of $U_x = 0.6U_b$ were not detected by any of the probes measuring this response. Additionally, the swirl prevented the reattachment of the jet; therefore, in the near region, the measured velocity values were close to zero, or even negative, due to the lengthening of the internal recirculation zone (see R-1.1). For these reasons, the effect of P4* was conveniently represented in response R-1.3.

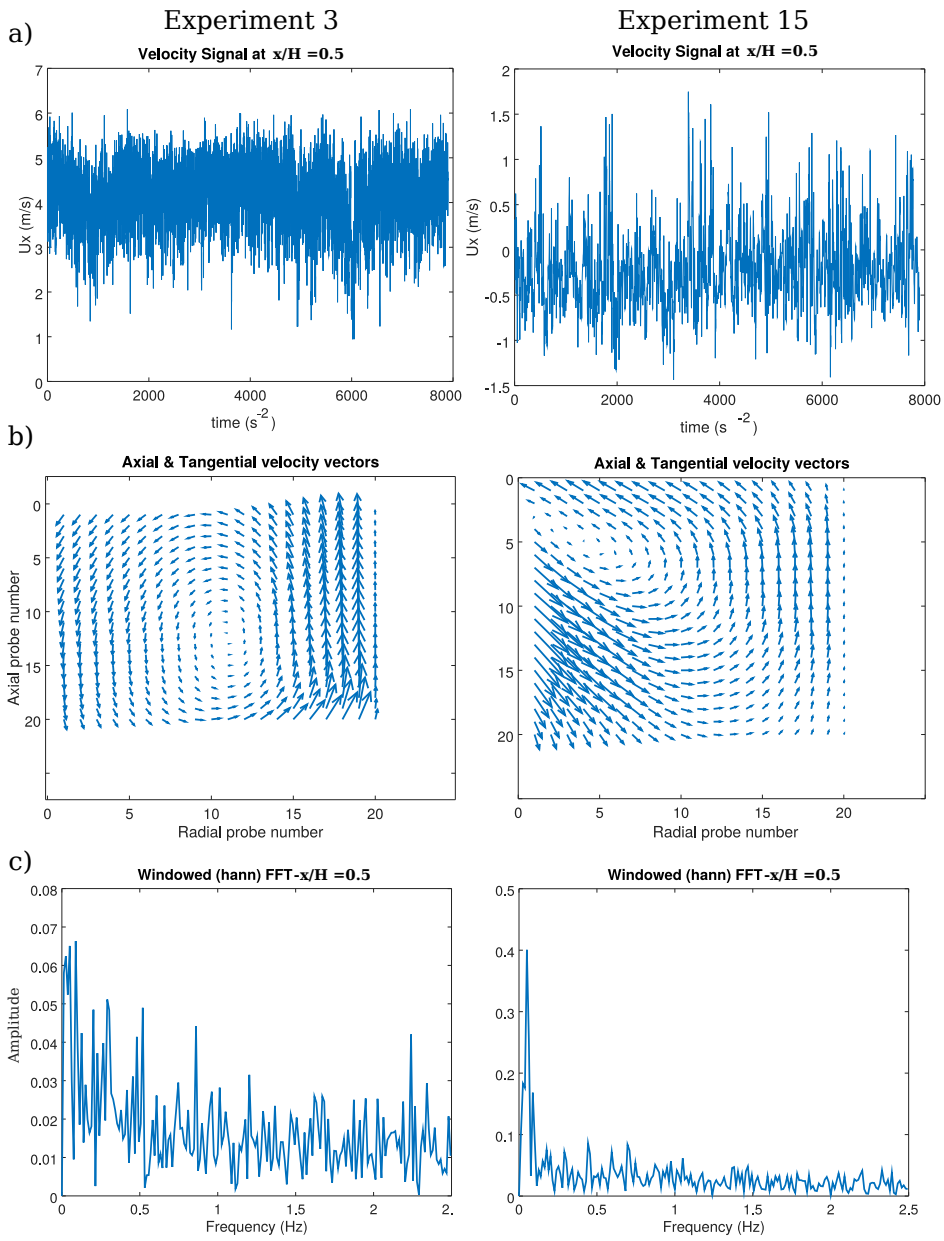


**Figure 5.** Some examples of sampled data for Experiments 3 and 15; (**a**) measured $U_x$ over the axis at $x/H = 0.5$; (**b**) 2D velocity vectors obtained by averaging the recirculation zone data (R-2); (**c**) FFT of the $U_x$ data presented in a).

Among the studied parameters, only P1* had a statistically significant effect on the physical $(x/R)$ and normalized $(x/H)$ distances. Regarding the physical distance $(x/R)$, a slightly higher decay of the main jet up to this velocity was present in the tall-form dryers. Normalizing this distance $(x/H)$ showed that with respect to the height of the chamber, the decay distance was significantly higher in short-form dryers (P1* = 1.2). Therefore, the jet passed through a larger portion of the chamber before losing energy. This may occur because in short-form chambers a stronger recirculation zone is created (see R-2.1), which subtracts more energy from the jet.

4.3.3. R-1.3—Jet Penetration Inside the Drying Chamber: Normalized Velocity ($U_x/U_b$ at 0.5 $x/H$)

For this response, the P4* factor had a strong effect in reducing jet penetration (see Figure 6b). Similar results were reported by Langrish et al. [14], where the jet behavior

changed from a fast-flowing core without swirl to becoming shortened when a small amount of swirl was included (15°). From this, it is inferred that for P-1.2 it was impossible to measure the effect of P4* because the decay rate of the jet was very high. This higher jet decay indicates a stronger interaction between the air and the atomized product, which is a desirable aspect from a thermal efficiency point of view, but not for the accumulation of the product on the chamber walls, as discussed in Southwell and Langrish [28]. Very close to the statistical significance line is the parameter P1*. This implies that the jet velocity in the axial center of the drying chamber is lower in a long-form chamber than in a short-form one. While this can be related to reduced particle residence times in the short-form dryer, larger P1* values increase the strength of the recirculating flow, which may lead to significant differences among the individual residence times.

R-1.1 - Length $x/R$ of the inner recirculation vortex ($U_x = 0$)

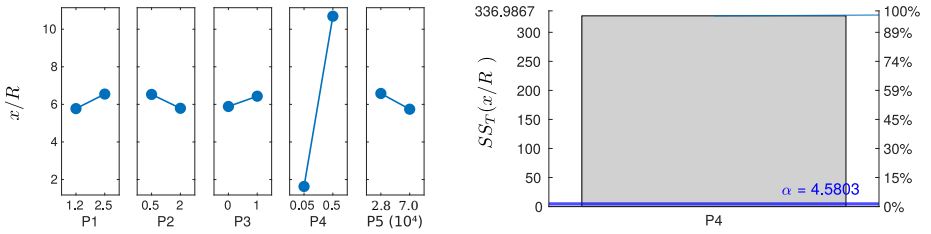


R-1.2 - Distance $x/R$ for the jet to decay to $0.6U_b$

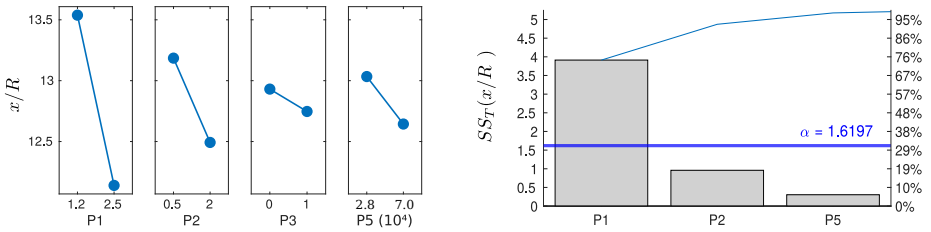


R-1.4 - *rms* fluctuations of the axial velocity at $x/R$ = 10

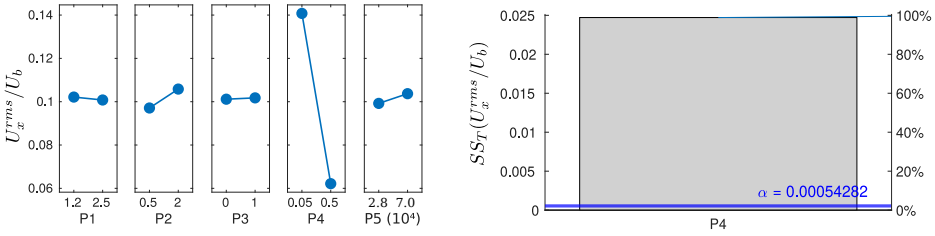


R-2.4 - Position $x/R$ of the recirculation vortex

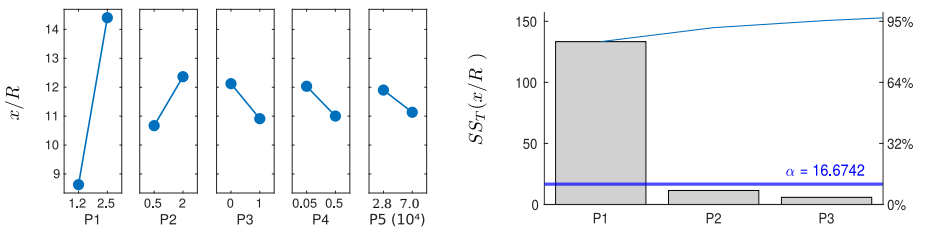


(**a**) Response variables related to a physical distance $(x/R)$.

**Figure 6.** *Cont.*

R-1.1 - Length $x/H$ of the inner recirculation vortex ($U_x = 0$)

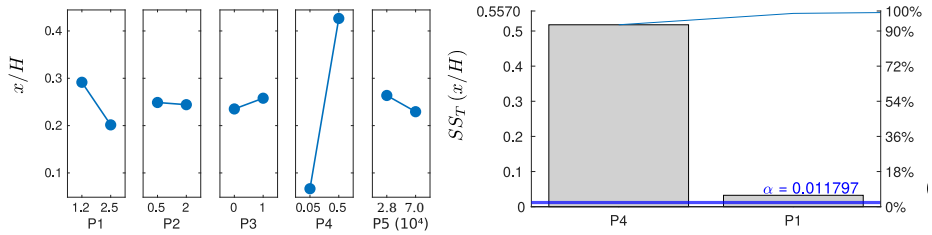


R-1.2 - Distance $x/H$ for the jet to decay to $0.6U_\mathrm{b}$

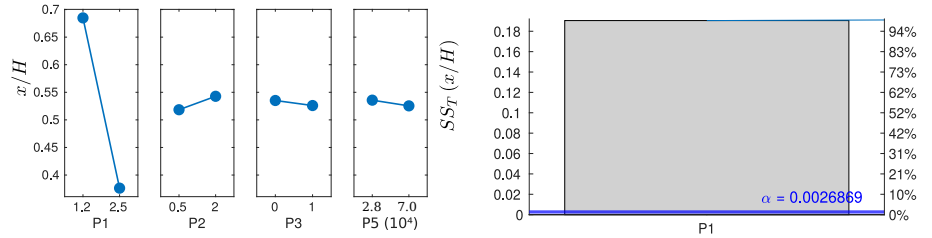


R-1.3 - Jet penetration inside the drying chamber $U_x/U_b$ @ $x/H = 0.5$

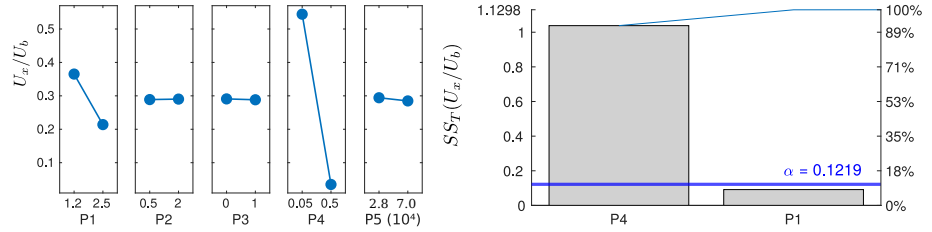


R-1.4 - rms fluctuations of the axial velocity at $x/H = 0.5$

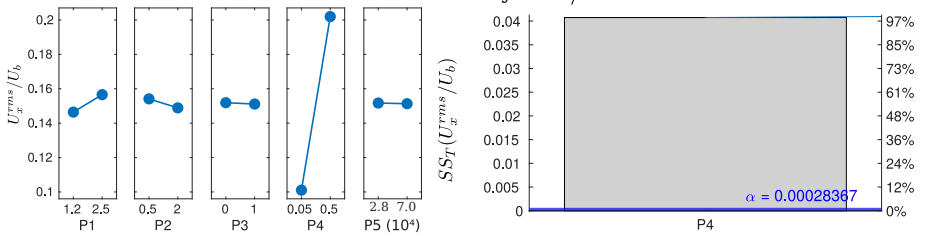


(**b**) Normalized responses in the main jet (R-1.1 to R-1.4).

R-1.5-1 - Dominant frequency (Hz) at $x/H = 0.5$

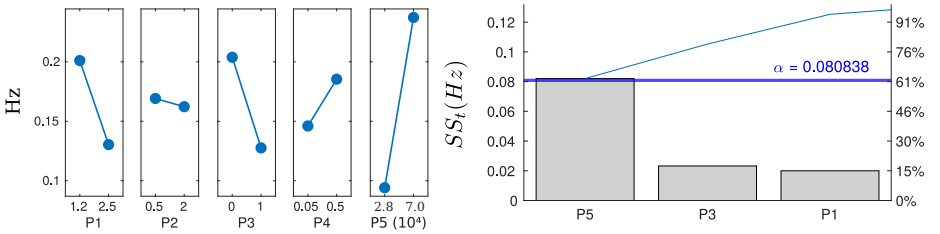


R-1.5-2 - Amplitude (m) at $x/H = 0.5$

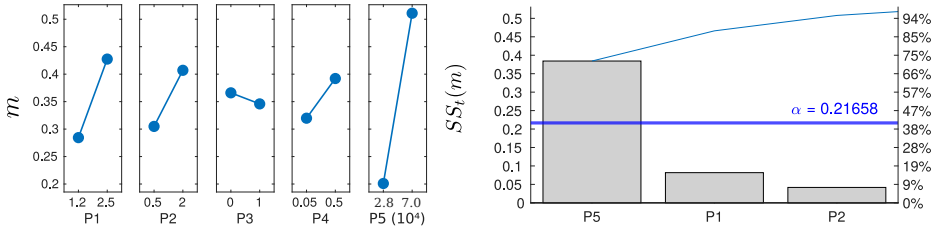


(**c**) Responses in the main jet associated with precession (R-1.5).

**Figure 6.** *Cont.*

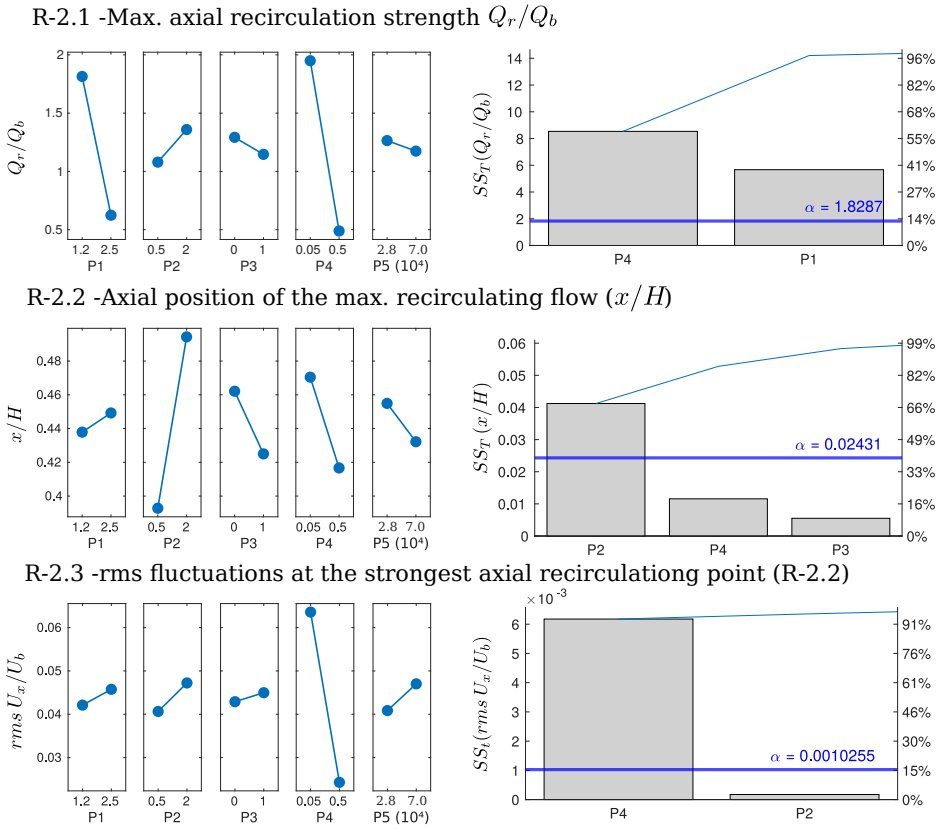


(**d**) Normalized responses in the recirculation zone (R-2).

**Figure 6.** Factor effects analysis of the influence of factor parameters on the response variables. **Left** column: main effects plot showing the mean response value for each level of the two-level factor; **right** column: Pareto chart of the standardized main effects. The horizontal blue line defines the 95% confidence interval ($P$ = 0.05). The value of $\alpha$ represents the threshold value in the response variable for this confidence interval. $SS_T$ represents the sum of the squares.

#### 4.3.4. R-1.4—*rms* Fluctuations of the Axial Velocity at $x/R = 10$ and at $x/H = 0.5$

The responses for the physical ($x/R = 10$) and normalized ($x/H = 0.5$) distances are presented in Figure 6a,b. For a fixed downstream position of the discharge ($x/R = 10$), P4* was the only parameter generating a significant response, increasing the magnitude of the *rms* fluctuations of the axial velocity ($rms\,U_x/U_b$) by 100%. This indicates that high swirl numbers increased the instabilities in the near-field of the jet and increased the mixing rate. At the normalized position $x/H = 0.5$, P4* was again the only parameter with a significant response. However, in this case, higher values of P4* generated a substantial decrease in $rms\,U_x$ values. Similar results were reported by Southwell and Langrish [28] near $x/H = 0.5$. This significant increase in the R-1.4* response was likely associated with a precessing motion of the jet around the measured position and a more substantial decay rate.

#### 4.3.5. R-1.5.1—Dominant Frequency (Hz) at the Normalized Position $x/H = 0.5$

The only parameter significantly affecting this response was P5*, increasing the dominant frequency (Hz) values (see Figure 6c). A similar conclusion was reached in Woo et al. [16], which stated that higher inlet velocities tend to magnify the jet-feedback mechanism, resulting in more uneven pressure gradients and accelerating the precessing motion of the jet. The maximum obtained ranges for the dominant frequency (R-1.5.1) were comparable to those measured in computational and experimental studies conducted by other authors [14,15,23] under similar swirl numbers. Among the parameters with weak

responses were P3* and P1*. In the case of higher P1* values, the decrease in the dominant frequency of the center current was likely because, in long-form chambers, the pressure gradients became smaller. In contrast with the trend observed with many other response variables, P4* did not have a statistically significant effect, with an average increase of 30% in dominant frequency from P4* = 0.05 to 0.5. Lebarbier et al. [15] reports a 40% increase in the frequency value from P4* = 0 to 0.4, being the most significant increase (32%) from P4* = 0 to 0.25. This may indicate that P4* is only relevant under low swirl values.

#### 4.3.6. R-1.5.2—Amplitude (m) of the Dominant Frequency

For this response, P5* was again the only statistically significant parameter, having a proportional effect on the amplitude of the dominant frequency (see Figure 6c). At higher Reynolds numbers, the pressure imbalance in the periphery of the jet increased, amplifying the deflection of the jet. Among the factors with weak responses were P1* and P2*. Regarding the effect of P1*, multiple factors may explain the increase in amplitude. For example, in narrow spray chambers, the measurement position $x/H = 0.5$ is located farther away from the discharge than in a short-form spray drying chamber, resulting in a larger amplitude measurement for the same oscillatory motion. However, using a fixed measurement position (0.9 m from the discharge), Woo et al. [16] reported an increase in the amplitude of the precessing motion when comparing a narrow spray chamber to a short-form chamber. This means that the measurement distance may not be the only factor influencing this response. Regarding P2*, the probable explanation for the amplitude increase with larger P2* values (the cylindrical section being longer than the conical section) was the resulting radially larger area to develop instabilities, feeding the precessing motion of the jet. Large amplitudes in the precessing motion of the jet are not desirable, as jet deflection may lead to increased particle deposition on the walls.

#### 4.3.7. R-2.1—Maximum Axial Recirculation Strength ($Q_r/Q_b$)

R-2-2 has two statistically significant parameters in its response: P4* and P1*. As P4* decreased, the jet penetration (R-1.3) increased, and a stronger recirculation flow was induced (see Figure 6d). This result differs from the findings presented in Southwell and Langrish [28], where it is mentioned that a higher swirl number generates a higher recirculation velocity in the vicinity of the walls and hence a higher recirculation flow. According to the results of this study, this is analyzed differently since the recirculation flow is affected by the jet expansion. Figure 5b illustrates this by comparing the results of Experiment 3 (P4* = 0.05) with those of Experiment 15 (P4* = 0.5). For Experiment 15, the jet had excessive dispersion in the radial direction, which reduced the space to form the recirculation vortex, so it did not have the same strength as for Experiment 3. Regarding P1*, it was observed that short-form chambers generate a stronger recirculation flow than long-form chambers. The possible reason is that there is more space to develop the recirculation zone in these chambers. A stronger recirculation zone will increase the difference in residence time between the atomized particles since some will not leave the chamber immediately but will remain in this zone for some time.

#### 4.3.8. R-2.2—Axial Position of the Max. Recirculating Flow ($x/R$ & $x/H$)

Regarding the physical position from the discharge ($x/R$), it was observed that P1* was the only parameter with a significant response, as presented in Figure 6a. This means that in tall-form dryers, the recirculation zone is formed further away from the jet discharge. When the position of R-2.2 was normalized to the chamber height ($x/H$), P2* became the only significant parameter (see Figure 6d). In this case, P1* did not present a significant response since the recirculation zone moved away from the discharge by making the chamber taller (P1* = 2.5). However, it maintained more or less the same relative position to

its height. The practical implications of this parameter should be analyzed in conjunction with P3* since recirculated particles may impact the wall in the shape-change zone (conical to cylindrical).

#### 4.3.9. R-2.3—*rms* Fluctuations of the Axial Velocity at the Recirculation Vortex (R-2.4—$x/H$)

The only significant parameter for this response was P4* (swirl number), as presented in Figure 6d. Increasing this parameter had a marked stabilizing effect on the recirculation zone. This behavior should have several implications for the accumulation and detachment of particles on the chamber walls; therefore, it should be addressed in future studies.

#### 4.3.10. Spreadsheet of Main Effects

Table 6 presents a summary of the effects of the design parameters on the normalized responses. For the center jet region (R-1.1 to R-1.4), parameters P1* and P4* were the only ones with statistically significant responses. For the response variables measuring the jet precessing behavior (R-1.5), parameter P5* was the only one with a significant response, which was observed for both the precession frequency (R-1.5.1*) and the amplitude (R-1.5.2*). For the recirculation zone (R-2), it was observed that the recirculation flow (R-2.1*) was directly affected by P1* and P4*, while the position of the recirculation flow depended mostly on P2*. Finally, the *rms* fluctuations of the recirculation zone (R-2.3*) were directly affected by P4*, whereas the response of the other parameters was not statistically significant.

**Table 6.** Spreadsheet summarizing the results of the main effects plots. Dark blue: statistically significant responses ($p$-value < 0.05); light blue: other responses with lower statistical significance (0.10 > $p$-value > 0.05).

| **Flow Region** | **Main Jet Region (R1)** | | | | | | **Recirculation Region (R2)** | | |
|---|---|---|---|---|---|---|---|---|---|
| | 1.1* | 1.2* | 1.3* | 1.4* | 1.5.1* | 1.5.2* | 2.1* | 2.2* | 2.3* |
| ine **P1*** | | | | | | | | | |
| **P2*** | | | | | | | | | |
| **P3*** | | | | | | | | | |
| **P4*** | | | | | | | | | |
| **P5*** | | | | | | | | | |

### *4.4. Curvature in the Response*

Figure 7 presents the main effect plots for the normalized responses in regions R-1 and R-2, including intermediate parameters (Experiment 17), allowing the visualization of the curvature in the response. The parameters with statistically significant responses in the main effects plot (Figure 6) have been highlighted within a blue box. Since only one center point experiment was conducted, the response of non-statistically significant parameters was greatly affected by that of the significant parameter(s). Further experiments with partial center points would be required to study curvature responses in less significant parameters.

For the central zone (Figure 7a), it was observed that the swirl number (P4*) had a very strong effect on the jet penetration (R-1.3). This was exemplified in the P4* [0.05, 0.275] interval, where a reduction of about 500% in R-1.3 ($U_x/U_b$) was observed. Similar results of the sensitivity of jet decay to swirl number are discussed inLangrish et al. [14]. In contrast, for R1-4* (*rms* $U_x$ @ $x/H = 0.5$), depicted in Figure 7b, the effect of P4* was initially insignificant but became more relevant after the intermediate point, increasing the response by 100%.

Regarding responses associated with the effect of P5* on the precessing motion of the jet (R-1.5), a concave upwards response was observed for both the dominant frequency (R-1.5.1) and amplitude (R-1.5.2). The concavity was much more evident for the dominant frequency (see Figure 7c). This is because P5* was barely over the significance threshold ($p$-value = 0.05 in Figure 6c), so its center point response could be affected by other parameters with weak responses, such as P3* and P1*. These parameters generated a response in the reverse direction to P5*; therefore, additional experiments may be required to be confident of the curvature in this response. For the amplitude of the dominant frequency (R-1.5.2), presented in Figure 7d, there was more certainty in interpreting the result since P5* was more statistically significant in this case. Moreover, the weak factors (P1* and P2*) presented the same response direction in this case. Still, in the first interval (P5* = 2.8 to P5* = 4.2), there was no change in the response, only becoming significant after the midpoint, with an increase close to 150% at P5* = 7.0. In real-life applications, increasing the volumetric flow of drying air above a certain threshold is not convenient. Under the current configuration, this threshold represented a fill time lower than 11.64 s and a bulk velocity higher than 8.05 m/s at the discharge. These threshold values may be different when modifying the geometrical parameters of the annular jet and varying the chamber size, with this being an interesting issue to be addressed in future studies.

For the recirculation zone (R-2), the normalized recirculation flow rate (R-2.1) had a response that tended to be negatively proportional to P1* and P4* (see Figure 7e), although in the case of P1*, the curvature was more apparent. In this case, both P1* and P4* generated statistically significant responses, and the noise of the other parameters was minimal. Regarding the position of the recirculation zone (R-2.2), presented in Figure 7f, the effect of P2* generated a concave upwards curve, with no significant change in position between P2* = 0.5 to P2* = 1.25. This could indicate that at P2* = 1.25, the conical section of the chamber still affected the recirculation zone development, influencing its positioning. However, this response may also be related to the weak parameters (P3* and P4*), which had an opposite response direction. For the stability of the recirculation zone (R-2.3), which was presented in Figure 7g, there was a concave downward behavior, which indicates that the stability in the recirculation zone depended on P4* crossing a certain threshold between P4* = 0.275 and P4* = 0.5.

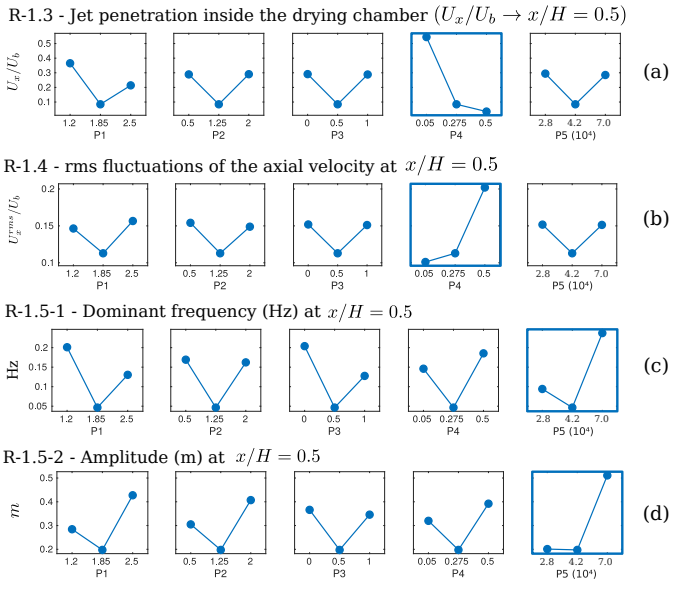


(**A**) Main jet region.

**Figure 7.** *Cont.*

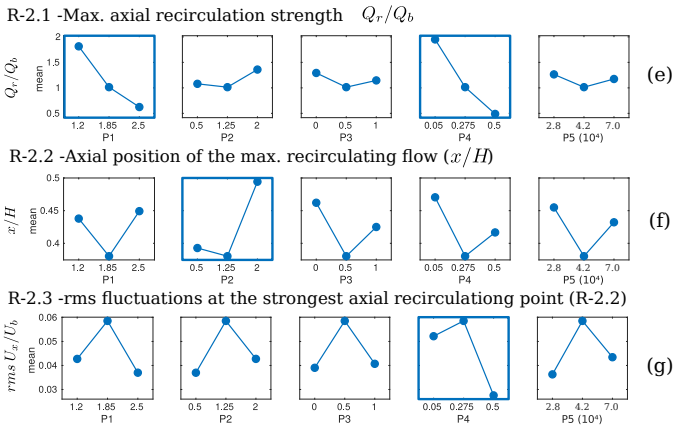


(**B**) Recirculating region.

**Figure 7.** Main effects plot including center point results (Experiment 17) in the main jet (R-1) and the recirculation region (R-2).

## 5. Conclusions

This study employs Computational Fluid Dynamics (CFD) and Design of Experiments (DOE) methods to analyze the parametric effects of some geometrical design parameters of a spray drying chamber on internal airflow dynamics. The cost-effective CFD approach adopted here, evaluated in previous studies [24,27], incorporates mesh adaptation and allows for full 3D transient simulations of spray dryers with turbulence resolution capabilities at relatively low computational costs.

This study has two main contributions: the proposed methodology and the type of results obtained. First, regarding the methodology, this work highlights and reinforces the feasibility of conducting transient parametric CFD studies for spray drying applications. Future research can adopt similar methodologies and build on the CFD models used in this study to expand simulations to the complete spray drying process (including particle atomization and evaporation), evaluate a broader range of geometrical and operational parameters, scale the process, perform "what-if" analyses, and model different types of drying equipment (e.g., counter-current or side-feed systems).

Second, regarding the results obtained, the most notable findings are the parameter–response relationships identified between geometric factors and airflow dynamics. Unlike previous studies that contemplated qualitative response variables, this study assumed the challenge of incorporating quantitative dependent variables (responses). These variables encompass various aspects of the internal flow dynamics within the dryer, enabling a deeper understanding of the complex internal flow behavior and its potential interactions with the particle phase. By combining the CFD approach with the DOE methodology into a parametric study, to the best of the authors' knowledge, this study is the first of its kind in the field of spray drying simulations.

Concerning the influence of various parameters and the potential reduction in the number of factors, the results of this study lead to several conclusions. It was found that the main design parameters are the swirl number at the jet discharge (P4*) and the chamber height-to-width ratio (P1*). By varying these parameters, the magnitude of most responses associated with flow dynamics can be modulated, making them highly relevant for spray dryer design. For existing equipment, where modifying the chamber height-to-width ratio (P1*) is not feasible, it is more practical to adjust the swirl angle by modifying the diffuser vanes. This opens the possibility of optimizing this parameter for different operating conditions. For the other two geometric parameters, the cylindrical-to-conical section height ratio (P2*) and the curvature in the conical section (P3*), the effects were generally weaker. However, some substantial responses were observed, particularly for

R-2.2 (the axial position of the recirculating vortex) and for R-1.4 and R-1.5, which describe the precessing motion of the central jet. These results suggest that these parameters could influence the formation of the recirculation zone, where the jet reverses direction, potentially causing impingement with the chamber walls. In particle-laden flows, this behavior could result in particles impacting the walls, exiting the chamber directly through the bottom, or recirculating upward, thereby affecting product accumulation on the walls and particle residence times. These potential effects have been proposed in previous studies [5,13]. Thus, these parameters should be considered in future studies that include particle atomization and drying.

For the last parameter, P5*, which represents the Reynolds number, a very strong influence was observed on the precessing motion of the central jet. As P5* increased—and consequently, the volumetric flow rate and drying capacity of a real unit—the main precession frequency of the central jet also increased, along with its amplitude (R-1.5.1 and R-1.5.2). This effect appears to follow a curved response: it was dampened at low and medium ranges of P5*, with a significant increase at the highest range evaluated. Similarly to the geometric parameters P2* and P3*, jet precession is associated with particle accumulation and jet impingement on the chamber walls. From a practical standpoint, this suggests the need to limit the power of the suction blower (which generates the negative pressure driving airflow into the chamber) when drying heat-sensitive products. Additionally, the ideal volumetric flow rate may vary depending on the specific drying chamber topology.

**Author Contributions:** Conceptualization, J.A.G.S. and C.H.G.U.; Methodology, J.A.G.S., A.G.M., and C.H.G.U.; Resources, A.G.M.; Supervision, A.G.M. and C.H.G.U.; Software, J.A.G.S. and C.H.G.U.; Validation, J.A.G.S.; Writing, J.A.G.S., A.G.M. and C.H.G.U.; Review and Editing, A.G.M. and C.H.G.U. All authors have read and agreed to the published version of the manuscript.

**Funding:** J.A. Gutiérrez acknowledges a PhD Scholarship from COLCIENCIAS (PDBCNal, COLDOC-Convocatoria 647).

**Data Availability Statement:** Data on the response variables and the OpenFOAM solver will be available upon reasonable request.

**Acknowledgments:** The authors wish to thank the CTTC—Centre Tecnològic de Transferència de Calor—Universitat Politècnica de Catalunya and Assensi Oliva, for their support in economic, computational, and physical resources for the development of this study.

**Conflicts of Interest:** The authors declare no conflicts of interest.

## References

1. Kieviet, F. Modelling Quality in Spray Drying. Ph.D. Thesis, Eindhoven University of Technology, Eindhoven, The Netherlands, 1997.
2. Anandharamakrishnan, C.; Gimbun, J.; Stapley, A.G.F.; Rielly, C.D. A study of particle histories during spray drying using computational fluid dynamic simulations. *Dry. Technol.* **2010**, *28*, 566–576. [CrossRef]
3. Keshani, S.; Daud, W.R.W.; Nourouzi, M.; Namvar, F.; Ghasemi, M. Spray drying: An overview on wall deposition, process and modeling. *J. Food Eng.* **2015**, *146*, 152–162.
4. Zbicinski, I. Modeling and scaling up of industrial spray dryers: A review. *J. Chem. Eng. Jpn.* **2017**, *50*, 757–767. [CrossRef]
5. Huang, L.; Kumar, K.; Mujumdar, A. A parametric study of the gas flow patterns and drying performance of co-current spray dryer: Results of a computational fluid dynamics study. *Dry. Technol.* **2003**, *21*, 957–978. [CrossRef]
6. Kadja, M.; Bergeles, G. Modelling of slurry droplet drying. *Appl. Therm. Eng.* **2003**, *23*, 829–844. [CrossRef]
7. Roustapour, O.; Hosseinalipour, M.; Ghobadian, B.; Mohaghegh, F.; Azad, N. A proposed numerical–experimental method for drying kinetics in a spray dryer. *J. Food Eng.* **2009**, *90*, 20–26. [CrossRef]
8. Wu, Z.; Mujumdar, A. A parametric study of spray drying of a solution in a pulsating high-temperature turbulent flow. *Dry. Technol.* **2006**, *24*, 751–761. [CrossRef]
9. Phisut, N. Spray drying technique of fruit juice powder: Some factors influencing the properties of product. *Int. Food Res. J.* **2012**, *19*, 1297–1306.

10. Fletcher, D.; Guo, B.; Harvie, D.; Langrish, T.; Nijdam, J.; Williams, J. What is important in the simulation of spray dryer performance and how do current CFD models perform? *Appl. Math. Model.* **2006**, *30*, 1281–1292. [CrossRef]
11. Guo, B.; Langrish, T.; Fletcher, D.F. Simulation of turbulent swirl flow in an axisymmetric sudden expansion. *AIAA J.* **2001**, *39*, 96–102. [CrossRef]
12. Huang, L.; Kumar, K.; Mujumdar, A. Use of computational fluid dynamics to evaluate alternative spray dryer chamber configurations. *Dry. Technol.* **2003**, *21*, 385–412. [CrossRef]
13. Keshani, S.; Montazeri, M.H.; Daud, W.R.W.; Nourouzi, M.M. CFD modeling of air flow on wall deposition in different spray dryer geometries. *Dry. Technol.* **2015**, *33*, 784–795. [CrossRef]
14. Langrish, T.; Williams, J.; Fletcher, D. Simulation of the effects of inlet swirl on gas flow patterns in a pilot-scale spray dryer. *Chem. Eng. Res. Des.* **2004**, *82*, 821–833. [CrossRef]
15. Lebarbier, C.; Kockel, T.; Fletcher, D.; Langrish, T. Experimental measurement and numerical simulation of the effect of swirl on flow stability in spray dryers. *Chem. Eng. Res. Des.* **2001**, *79*, 260–268. [CrossRef]
16. Woo, M.W.; Daud, W.R.W.; Mujumdar, A.S.; Wu, Z.; Talib, M.Z.M.; Tasirin, S.M. Non-swirling steady and transient flow simulations in short-form spray dryers. *Chem. Prod. Process Model.* **2009**, *4*, 20. [CrossRef]
17. Anandharamakrishnan, C. In *Computational Fluid Dynamics Applications in Food Processing*; Springer: New York, NY, USA, 2013. [CrossRef]
18. Woo, M.; Che, L.; Daud, W.R.W.; Mujumdar, A.; Chen, X. Highly swirling transient flows in spray dryers and consequent effect on modeling of particle deposition. *Chem. Eng. Res. Des.* **2012**, *90*, 336–345. [CrossRef]
19. Pawar, S.K.; Abrahams, R.H.; Deen, N.G.; Padding, J.T.; van der Gulik, G.J.; Jongsma, A.; Innings, F.; Kuipers, J. An experimental study of dynamic jet behaviour in a scaled cold flow spray dryer model using PIV. *Can. J. Chem. Eng.* **2014**, *92*, 2013–2020. [CrossRef]
20. Masters, K. *Spray Drying Handbook*; Longman Scientific & Technical: Iver, UK, 1991; ISBN 9780470217436.
21. Mujumdar, A. *Handbook of Industrial Drying*; CRC Press: Boca Raton, FL, USA, 2014.
22. Nijdam, J.J.; Guo, B.; Fletcher, D.F.; Langrish, T. Lagrangian and Eulerian models for simulating turbulent dispersion and coalescence of droplets within a spray. *Appl. Math. Model.* **2006**, *30*, 1196–1211. [CrossRef]
23. Fletcher, D.; Langrish, T. Scale-adaptive simulation (SAS) modelling of a pilot-scale spray dryer. *Chem. Eng. Res. Des.* **2009**, *87*, 1371–1378. [CrossRef]
24. Gutiérrez Suárez, J.A.; Galeano-Urueña, C.H.; Gómez-Mejía, A. Adaptive Mesh Refinement Strategies for Cost-Effective Eddy-Resolving Transient Simulations of Spray Dryers. *ChemEngineering* **2023**, *7*, 100. [CrossRef]
25. Sommerfeld, M. Modelling requirements for CFD calculations of spray dryers. In Proceedings of the Jornada em Escoamentos multifásicos, Campinas, Brazil, 23–27 March 2015.
26. Lampa, A.; Fritsching, U. Large Eddy Simulation of the spray formation in confinements. *Int. J. Heat Fluid Flow* **2013**, *43*, 26–34. [CrossRef]
27. Gutiérrez Suárez, J.A.; Galeano-Urueña, C.H.; Gómez-Mejía, A. Low-Cost Eddy-Resolving Simulation in the Near-Field of an Annular Swirling Jet for Spray Drying Applications. *ChemEngineering* **2021**, *5*, 80. [CrossRef]
28. Southwell, D.; Langrish, T. The effect of swirl on flow stability in spray dryers. *Chem. Eng. Res. Des.* **2001**, *79*, 222–234. [CrossRef]
29. Coleman, D.E.; Montgomery, D.C. A systematic approach to planning for a designed industrial experiment. *Technometrics* **1993**, *35*, 1–12. [CrossRef]
30. Rhew, R.D.; Parker, P.A. A parametric geometry computational fluid dynamics (CFD) study utilizing design of experiments (DOE). *Am. Insitute Aeronaut. Astronaut. (AIAA)* **2007**, *1615*, 2007.
31. Carić, M. *Concentrated and Dried Dairy Products*; VCH Publishers Inc.: New York, NY, USA, 1994.
32. Mujumdar, A.; Huang, L.; Chen, X. An overview of the recent advances in spray-drying. *Dairy Sci. Technol.* **2010**, *90*, 211–224. [CrossRef]
33. García-Villalba, M.; Fröhlich, J.; Rodi, W. On inflow boundary conditions for large eddy simulation of turbulent swirling jets. In Proceedings of the 21st International Congress of Theoretical and Applied Mechanics, Warsaw, Poland, 15–21 August 2004.
34. Pawar, S. Multiphase Flow in a Spray Dryer: Experimental and Computational Study. Ph.D. Thesis, Technische Universiteit Eindhoven, Eindhoven, The Netherlands, 2014.
35. Huang, L.; Kumar, K.; Mujumdar, A. Simulation of a spray dryer fitted with a rotary disk atomizer using a three-dimensional computional fluid dynamic model. *Dry. Technol.* **2004**, *22*, 1489–1515. [CrossRef]
36. Gutiérrez Suárez, J.A. Modelación CFD y validación Experimental del Proceso de Evaporación de Agua en un Secador por Aspersión. Master's Thesis, Universidad Nacional de Colombia–Sede Bogotá–Facultad de Ingeniería–Ingeniería Mecánica, Bogotá, Colombia, 2015.
37. Kieviet, F.; Kerkhof, P. Air flow, temperature and humidity patterns in a co-current spray dryer: Modelling and measurements. *Dry. Technol.* **1997**, *15*, 1763–1773. [CrossRef]
38. Oakley, D. Spray dryer modeling in theory and practice. *Dry. Technol.* **2004**, *22*, 1371–1402. [CrossRef]

39. Hammad, K.J.; Milanovic, I.; Al-Masoud, N. Characteristics of a Confined Annular Jet Flow Field. In Proceedings of the ASEE Northeast Section Conference 2013, Northfield, VT, USA, 14–16 March 2013.
40. Southwell, D.; Langrish, T. Observations of flow patterns in a spray dryer. *Dry. Technol.* **2000**, *18*, 661–685. [CrossRef]
41. Ko, N.; Chan, W. Similarity in the initial region of annular jets: Three configurations. *J. Fluid Mech.* **1978**, *84*, 641–656. [CrossRef]
42. Montgomery, D.C. *Design and Analysis of Experiments*; John Wiley & Sons: Hoboken, NJ, USA, 2017.
43. Davidson, L. *Fluid Mechanics, Turbulent Flow and Turbulence Modeling*; Lecture notes; Chalmers University of Technology: Gothenburg, Sweden, 2015.
44. Spalart, P.R.; Deck, S.; Shur, M.L.; Squires, K.D.; Strelets, M.K.; Travin, A. A new version of detached-eddy simulation, resistant to ambiguous grid densities. *Theor. Comput. Fluid Dyn.* **2006**, *20*, 181. [CrossRef]
45. Travin, A.; Shur, M.; Strelets, M.; Spalart, P. Physical and numerical upgrades in the detached-eddy simulation of complex turbulent flows. In *Advances in LES of Complex Flows*; Springer: Dordrecht, The Netherlands, 2002; pp. 239–254. [CrossRef]
46. Holzmann, T. *Mathematics, Numerics, Derivations and OpenFOAM®*, 4th ed.; Holzmann CFD: Loeben, Germany, 2017.
47. Moukalled, F.; Mangani, L.; Darwish, M. Temporal Discretization: The Transient Term. In *The Finite Volume Method in Computational Fluid Dynamics*; Springer: Cham, Switzerland, 2016; pp. 489–533. [CrossRef]
48. Bathe, K.J.; Zhang, H. A mesh adaptivity procedure for CFD and fluid-structure interactions. *Comput. Struct.* **2009**, *87*, 604–617. [CrossRef]
49. Culpo, M. Current Bottlenecks in the Scalability of OpenFOAM on Massively Parallel Clusters. PRACE White Paper to Appear on http://www. praceri. eu. 2011. Available online: https://www.google.com.hk/url?sa=t&source=web&rct=j&opi=89978449&url=https://prace-ri.eu/wp-content/uploads/Current_Bottlenecks_in_the_Scalability_of_OpenFOAM_on_Massively_Parallel_Clusters.pdf&ved=2ahUKEwj17sLrg6-KAxWy0jQHHax_JK0QFnoECBUQAQ&usg=AOvVaw1V7ePKvi4mgI2CWrmqrAHz (accessed on 16 December 2024).